



## Article

# Ultra-Wideband Analog Radio-over-Fiber Communication System Employing Pulse-Position Modulation

Sandis Migla <sup>1</sup>, Kristaps Rubuls <sup>1</sup>, Nikolajs Tihomorskis <sup>1</sup>, Toms Salgals <sup>1</sup>, Oskars Ozolins <sup>1,2,3</sup>, Vjaceslavs Bobrovs <sup>1</sup>, Sandis Spolitis <sup>1</sup> and Arturs Aboltins <sup>1,\*</sup>

<sup>1</sup> Institute of Photonics, Electronics and Telecommunications, Riga Technical University, 12 Azenes Street, LV-1048 Riga, Latvia; sandis.migla@rtu.lv (S.M.); kristaps.rubuls@rtu.lv (K.R.); nikolajs.tihomorskis@rtu.lv (N.T.); toms.salgals@rtu.lv (T.S.); oskars.ozolins@rtu.lv (O.O.); vjaceslavs.bobrovs@rtu.lv (V.B.); sandis.spolitis@rtu.lv (S.S.)

<sup>2</sup> Department of Applied Physics, KTH Royal Institute of Technology, 10691 Stockholm, Sweden

<sup>3</sup> RISE Research Institutes of Sweden, 16440 Kista, Sweden

\* Correspondence: aboltins@rtu.lv

**Abstract:** This research presents a novel approach to 28 GHz impulse radio ultra-wideband (IR-UWB) transmission using pulse position modulation (PPM) over an analog radio-over-fiber (ARoF) link, investigating the impact of fiber-based fronthaul on the overall performance of the communication system. In this setup, an arbitrary waveform generator (AWG) is employed for PPM signal generation, while demodulation is performed with a commercial time-to-digital converter (TDC) based on an event timer. To enhance the reliability of transmitted reference PPM (TR-PPM) signals, the transmission system integrates Gray coding and Consultative Committee for Space Data Systems (CCSDS)-standard-compliant Reed-Solomon (RS) error correcting code (ECC). System performance was evaluated by transmitting pseudorandom binary sequences (PRBSs) and measuring the bit error ratio (BER) across a 5-m wireless link between two 20 dBi gain horn (Ka-band) antennas, with and without a 20 km single-mode optical fiber (SMF) link in transmitter side and ECC at the receiver side. The system achieved a BER of less than  $8.17 \times 10^{-7}$ , using a time bin duration of 200 ps and a pulse duration of 100 ps, demonstrating robust performance and significant potential for space-to-ground telecommunication applications.

**Keywords:** microwave communication; optical fiber communication; space communications; microwave photonics; energy efficiency; ultra wideband technology



Academic Editors: Darius Plonis and Andrius Katkevičius

Received: 4 March 2025

Revised: 4 April 2025

Accepted: 8 April 2025

Published: 11 April 2025

**Citation:** Migla, S.; Rubuls, K.; Tihomorskis, N.; Salgals, T.; Ozolins, O.; Bobrovs, V.; Spolitis, S.; Aboltins, A. Ultra-Wideband Analog Radio-over-Fiber Communication System Employing Pulse-Position Modulation. *Appl. Sci.* **2025**, *15*, 4222. <https://doi.org/10.3390/app15084222>

**Copyright:** © 2025 by the authors. Licensee MDPI, Basel, Switzerland. This article is an open access article distributed under the terms and conditions of the Creative Commons Attribution (CC BY) license (<https://creativecommons.org/licenses/by/4.0/>).

## 1. Introduction

With the advent of current 5G Advanced and future 6G networks [1], fronthaul solutions, such as radio-over-fiber (RoF), have gained prominence as a means of enhancing communication systems [2]. RoF employs optical fibers to create the fronthaul links for radio frequency (RF) signal transmission, offering a sizable usable bandwidth and low attenuation. Employment of RoF alleviates bandwidth constraints while enabling the distribution of antenna units (AUs) over longer distances without frequent amplification [3]. Additionally, RoF technology can support centralized processing and signal generation [4], reducing the complexity and power consumption of the entire network.

A promising RoF technology for 5G Advanced and 6G networks is ARoF [4]. In ARoF, an analog waveform modulates the optical transmitter, generating an analog optical signal transmitted through the fronthaul link. This approach minimizes the need for power-hungry, high-speed analog-to-digital converters (ADCs) and digital-to-analog converters

(DACs) compared to traditional digital interfaces [4], enabling the use of low-complexity and energy-efficient AUs. For these reasons, ARoF technology offers a spectrally efficient, power-efficient, and low-complexity solution. As next-generation networks plan to utilize even higher frequency bands, this becomes particularly important [2]. Consequently, ARoF technology has been explored in recent research for millimeter-wave [5,6] and terahertz links [7,8]. Additionally, ARoF is being considered for future distributed multiple-input multiple-output (D-MIMO) systems in 6G networks [4,9], which rely heavily on a distributed AU architecture to enhance wireless coverage.

Applications of ARoF technology include wireless communications, distributed sensor networks, radars, space communication systems, and many other applications [10]. In Figure 1, a visualization of the physical and wireless RF connections between the central office, base station, and user equipment is provided, depicting a communication system for remote sensing and space applications involving low Earth orbit, geostationary Earth orbit, and deep space satellites.

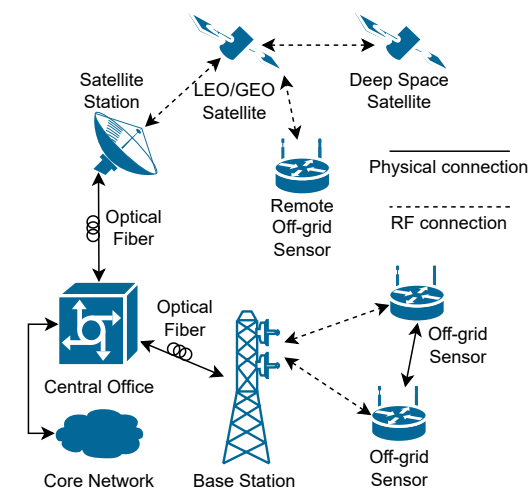


**Figure 1.** Usage scenarios for the proposed UWB ARoF technology.

ARoF is an increasingly popular solution for 5G Advanced and upcoming 6G telecommunication standards, leveraging millimeter-wave signals to support high-capacity broadband applications [11–13]. In [14], a hybrid architecture for 5G mobile networks based on the ARoF technological concept is described. The authors propose a long-range wireless communication solution with 1 km optical fiber and 20 m free-space optical communication (FSO) fronthaul, using quadrature amplitude modulation (QAM) signal with 700 MHz carrier, achieving 60 Mb/s data transmission rate.

The paper [15] demonstrates the seamless integration of ARoF with FSO and mm-wave wireless communication systems and shows satisfactory performance with QAM signals at simulated data transmission speeds exceeding 10 Gb/s.

ARoF technology can increase the performance of phased antenna arrays by using the modulation instability phenomenon [16]. The authors have demonstrated modulation instability gain of 38.1 dB by using 45 km long optical fiber. Another possibility is to use a single light source at the central office to achieve full duplex communication [17]. The presented system has achieved 2.5 Gb/s data transmission over 40 km long SMF.

Ultra-wideband (UWB) technology has emerged as a promising innovation for RF that allows for the use of ultra-short pulses for transmitting information, as well as applications in integrated sensing and communications (ISAC), radar technology, and distributed sensor networks [18].

Research on UWB modulation schemes [19,20] for use in ARoF communication systems has been conducted in the past. For example, paper [21] presents an UWB over fiber

communications system based on asymmetric Mach-Zehnder interferometer for optical modulation. It provides an overview of various UWB modulation schemes for use in ARoF systems, such as on-off keying (OOK), bi-phase modulation, pulse amplitude modulation, pulse shape modulation, and PPM. The authors have achieved error-free data transmission over a 20 km long SMF and 5 GHz wireless channel. In the paper [22], authors provide a performance evaluation of UWB signal transmission over SMF by using double-sided UWB and quasi single-sideband UWB (QSSB-UWB) monocycle pulses and analyzing the power spectral density of the signal at multiple transmission distances. The authors have found that QSSB-UWB pulses are more suitable for use with OOK and PPM. In paper [23], a low-complexity IR-UWB pulse generation method based on a linear combination of two monocycle pulses is presented, and transmission over SMF is evaluated. Error-free performance was achieved over 25 km long fiber at the speed of 2 Gb/s.

The PPM modulation scheme is widely used in RF and optical IR-UWB communication systems [24,25]. This modulation scheme encodes data as a time interval and allows ultra-short pulses to transmit data, increasing the power efficiency [26]. There are many types of PPM, such as coherent PPM, differential PPM, TR-PPM [27,28], variable PPM [29], overlap PPM and more [30]. Paper [31] proposes a nested PPM scheme for use in visible light communication systems, which simplifies the transmitter and receiver structure, therefore making nested PPM an attractive choice for a wide range of applications where energy efficiency and low cost are crucial.

Another application of PPM is in joint radar communication, which was experimentally validated with the employment of chirp sequences [32]. PPM transceiver can be set up as a joint radar communication system, using the receiving antenna unit as a radar. In this implementation, the transmitted signal will be locally used for symbol synchronization of the received waveform. Depending on the received reflections and pulses from other transmitters, distances and velocities of objects and receivers can be measured. This theoretical PPM communication system with radar capabilities will work as an ISAC system, adjusting, for example, the power of transmitted pulses, depending on the distance to the receiver, for power conservation purposes. In deep space communications, the position of a directional antenna may be adjusted, depending on the received pulses' power [33]. In terrestrial applications, PPM pulses may also be used for the localization of mobile objects, essentially working as a radar on top of the PPM communication [34].

This research presents a novel, experimentally validated communication system employing TR-PPM transmission over ARoF. In this research implementation, the central office is equipped with a local analog RoF transmitter; in turn, the base station consists of an remote antenna unit (RAU) serving as the RF transmitter in the access network. The demodulation of PPM signal is performed by TDC based on a commercial event timer. The presented system functions as a testbed for the investigation of IR-UWB communication and future use cases of UWB ISAC.

The manuscript is organized as follows: Section 2 discusses the use of PPM in ARoF applications, Section 3 describes the experimental setup used in this research, Section 4 shows the results of the conducted experiments, and finally, Section 5 provides conclusions about the presented research.

## 2. The Use of PPM

In this paper, TR-PPM is employed, where data are encoded by allocating pulses of duration  $\tau$  (s) into time bins of duration  $\Delta$  (s). Each of  $M = 2^b$  positions (time bins) represents a different symbol described by a predefined number of bits  $b$ . An additional reference pulse at the beginning of each frame helps to calculate the value of the received symbols. The first time bin starts after  $M \cdot \Delta + T_g$  seconds from the reference pulse, where

guard time, denoted as  $T_g$  (s), is introduced to ensure a safe interval between the pulses. This interval compensates for the hardware's inherent dead time, encompassing signal propagation delays and the duration required for processing. An example of a TR-PPM frame, which provides reference and symbol pulses with  $M = 4$  positions, is shown in Figure 2.

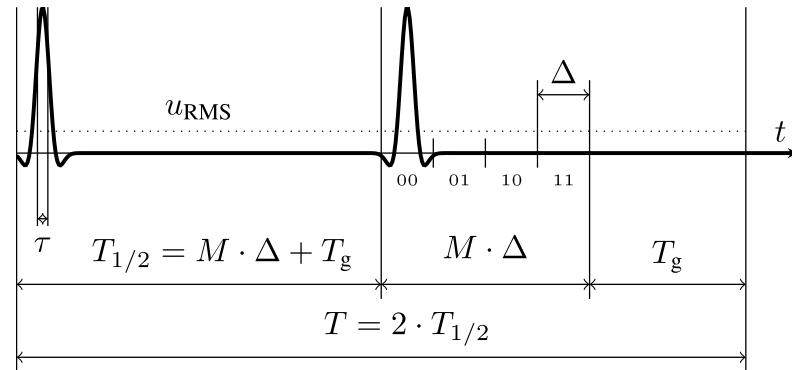


**Figure 2.** Example structure of one TR-PPM frame with  $M = 4$ .

The allocation of data symbols into the time between short pulses, measured in picoseconds (ps), significantly enhances energy efficiency per symbol. The root mean square (RMS) of the signal is defined as  $u_{\text{RMS}} = \sqrt{\int_0^{T/2} u(t)^2 dt}$ , where duration  $T_{1/2} = M \cdot \Delta + T_g$  and  $T = 2 \cdot T_{1/2}$  represent frame duration consisting of two halves of a TR-PPM symbol duration  $T_{1/2}$ , (s). The decrease in signal RMS  $u_{\text{RMS}}$ , achieved by using pulses with minimal pulse duration  $\tau$ , enables an increase in transmission distance while maintaining the same mean power consumption compared to conventional modulation schemes like OOK. By decreasing the time bins' width  $\Delta$ , more data in PPM can be allocated, increasing data transmission speed. It is worth noticing that although in some PPM applications, a simplified scheme with  $\Delta = \tau$  is used, the information is carried solely by the timing of the pulses' rising edges. Hence, the pulse width  $\Delta$  is not critical from an information-carrying perspective. However, pulse width affects both the link's energy efficiency and the signal's frequency bandwidth. Consequently, the narrower pulses create more energy-efficient transmission, whereas longer pulses require smaller bandwidth and are easier to detect. In the latter case, the pulse width shouldn't exceed guard time  $T_g$  to avoid overlapping the pulses.

As PPM encodes data in the time domain, precise time-to-digital conversion is essential for its demodulation. Ideally, each pulse has equal and constant amplitude and steep rising edge, allowing for pulse detection with a constant threshold that triggers precisely on one of the pulse's edges. As demodulation is performed by TDC, the precision of TDC significantly influences the speed of PPM communication. To avoid symbol errors, the time interval  $\Delta$  must be adjusted according to the TDC precision, ensuring that the measured time does not drift into adjacent pulse time bins.

Pulse threshold detection with precise time recording is what the Eventech Stream Time Tagger (ESTT) 7 Series event timer [35] provides. This event timer was used as TDC for PPM demodulation in previous papers [36,37], and it was also chosen as a TDC for PPM demodulation in this research. ESTT's time precision is around 1.5 ps with a dead time of 40 ns, which must be defined as the guard-time  $T_g$  in PPM.

Recently, a space-rated version of the ESTT—Eventech Space Ready Timing Module (ESRTM) was developed and is available for use in space applications where precise time measurement is needed [38]. ESRTM enables the implementation of a PPM receiver for Earth orbit and deep space satellites without the need to develop a dedicated system. ESRTM was launched with the European Space Agency's Hera mission [39] on 7 October 2024.

### 3. Experimental Setup

A series of captured experimental illustrations of the setup is shown in Figure 3. At the same time, a block diagram of the developed ARoF-based UWB communication system employing PPM is depicted in Figure 4, where the optical part is shown in red, the electrical part is displayed in blue, and the digital part is depicted in gray. The experimental system mainly consists of three parts: (a) ARoF transmitter, (b) RAU transmitter, and (c) RAU receiver. In the experimental setup, the following primary assumptions have been made: firstly, the radio channel is exclusive to our experiment; secondly, both the transmitter and receiver remain stationary; and, thirdly, multipath propagation effects are negligible due to the controlled environment. These assumptions align with the experimental constraints and ensure the system's performance is evaluated close to ideal conditions.

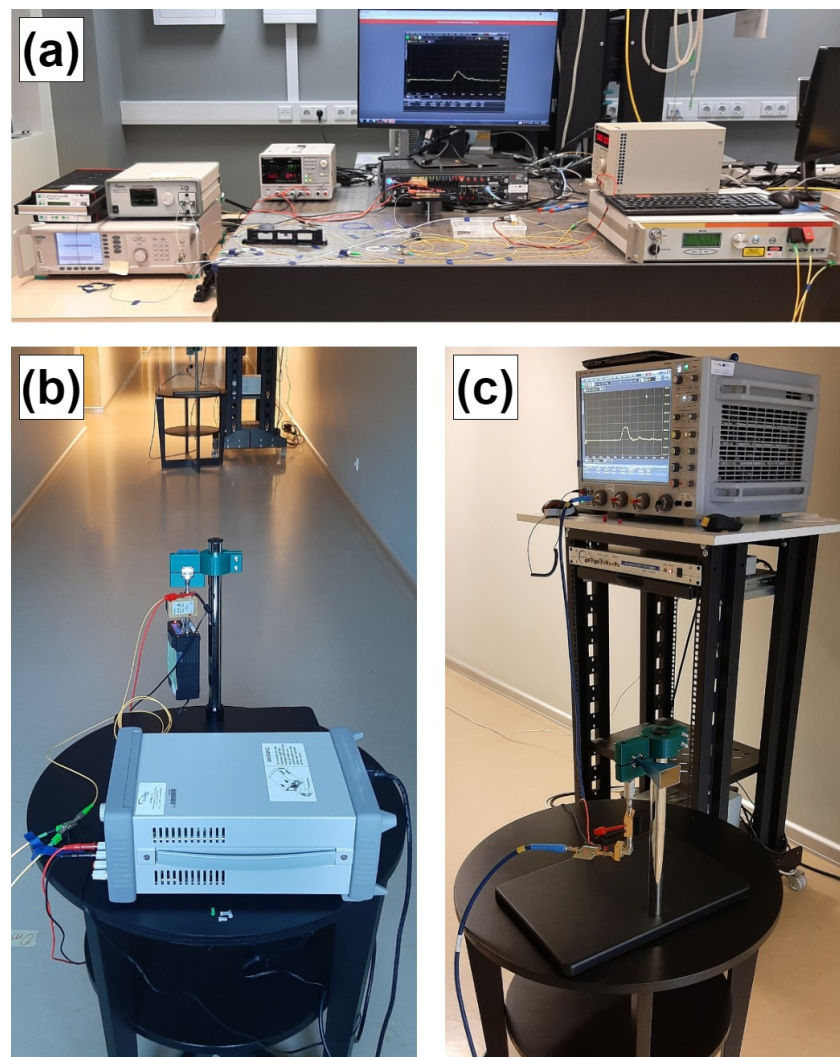


**Figure 3.** Captured experimental illustrations of ARoF-based UWB communication system employing PPM, (a) ARoF transmitter, (b) RAU transmitter, (c) RAU receiver.

#### 3.1. ARoF Transmitter

The optical output ( $\sim 1550$  nm wavelength) from the Cobrite DX-1 (ID Photonics, Neubiberg, Germany) continuous wave (CW) laser, with a linewidth of 25 kHz and an output power of +16 dBm, was first directly connected to a Mach-Zehnder modulator (MZM)—a 40 GHz MX-LN-40 intensity modulator (Exail Technologies, Paris, France) that has a 3.5 dB insertion loss and a 20 dB extinction ratio. The bias point was adjusted near its zero level. A sinusoidal signal generator MG3690C (Anritsu, Vienna, Austria), producing

a 14 GHz sinusoidal electrical signal (half of the proposed intermediate frequency), was directly connected to the electrical signal input of the first MZM. As a result, the desired RF of 28 GHz was achieved between the generated tones in the optical domain at the output of the first MZM. Polarization controllers were positioned before and after the first MZM to precisely adjust the polarization states of the optical signal during the experiment. The output of the first MZM, comprising two equal optical tones (carriers) spaced 28 GHz apart, was subsequently amplified using an erbium-doped fiber amplifier (EDFA) to compensate for optical power loss. The optical signal was then modulated with the TR-PPM waveform using a second MZM (Covega 10G, Jessup, MD, USA). The TR-PPM waveform was generated using the M8195A AWG (Keysight, Colorado Springs, CO, USA) with a 25 GHz analog bandwidth and a 65 GSa/s sampling rate. Due to the limited output power (maximum 1 V-pp) of the AWG, an RF broadband amplifier (SHF 100 BP, 17 dB gain, up to 25 GHz) was used to amplify the TR-PPM waveform before launching it into the RT input of the second MZM.

An optical signal pre-amplification by a second EDFA with an optimized gain was performed before launching the optical signal into a 20 km long ITU-T G.652 rec. compliant SMF span, which has 0.02 dB/km attenuation and a 17 ps/nm/km dispersion coefficient at 1550 nm.

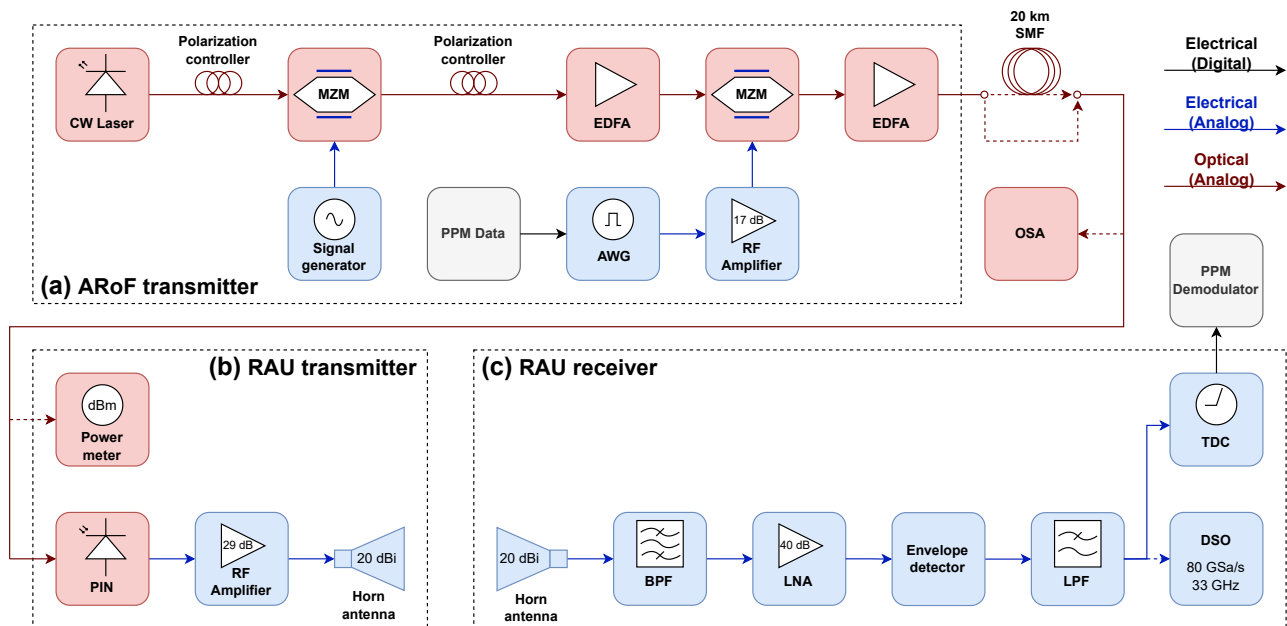


**Figure 4.** Experiment setup of ARoF-based UWB communication system employing PPM, (a) ARoF transmitter, (b) RAU transmitter, (c) RAU receiver.

### 3.2. RAU Transmitter

As for the optical receiver, a Discovery Semiconductors DSC10H p-i-n photodiode (PIN) with 50 GHz 3-dB electrical bandwidth with a sensitivity level +4 dBm for BER of  $10^{-12}$ , the dark current of 5 nA and responsivity of 0.65 A/W was used, which realized the photodetection-based RF generation from the optical beat-note. A broadband optical power meter and an optical spectrum analyzer were used at the end of the fiber line to measure and optimize the received optical power, which was later disconnected and replaced by the PIN after optimization. The optical spectra before the PIN can be seen in Figure 5. The RF signal output power from the PIN was limited. Therefore, the RF signal is amplified by a 38 GHz and +29 dB gain broadband amplifier (SHF 810) before being transmitted to the Ka-band (26.5–40 GHz) horn-type antenna with 20 dBi gain. Free space path loss of the transmitted 28 GHz signal at 5 m was 35.36 dB; at 10 m, it was 41.38 dB, and at 20 m it was

47.40 dB. As one can see from the calculations, the most critical insertion losses are at the beginning of the transmission distance.

In Figure 5, the Kerr nonlinear optical effects (NOE), e.g., the four-wave mixing (FWM) impact on the PPM modulated intermediate frequency optical signal, is illustrated, which affects the signal transmission through the optical distribution network. Additional spectrum peaks are caused by the high optical power level output ( $\sim +15$  dBm) of the second EDFA before launching the optical signal in the 20 km long SMF optical distribution network and are more pronounced than in the case of the back-to-back setup due to the nonlinear coefficient and the mode effective area of the SMF. Nevertheless, this does not significantly impact the BER, as NOE does not considerably affect PPM signals. The optical power of the three optical tones after the 20 km long SMF is about 3 dB lower due to the attenuation in the fiber.

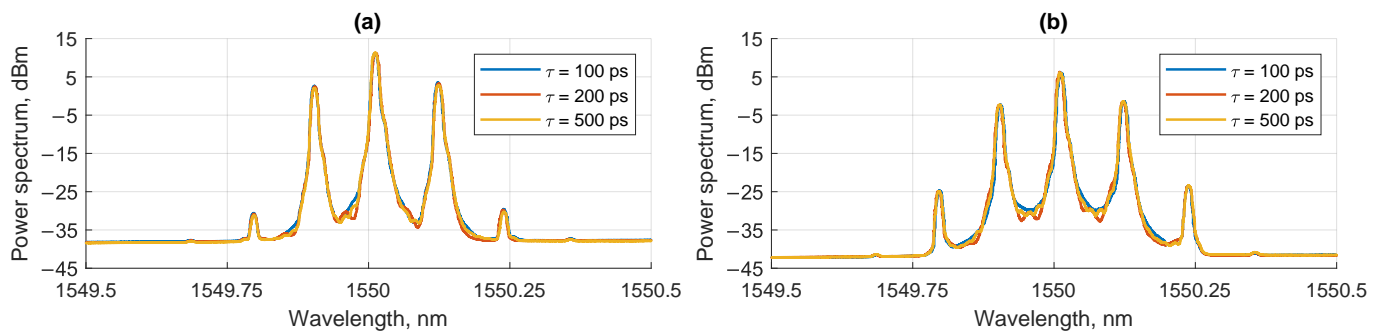


**Figure 5.** Optical spectrum before PIN for (a) back-to-back setup, (b) setup with 20 km SMF.

### 3.3. RAU Receiver

The receiver was located 5 m away from the RAU transmitter. The transmitted mm-wave signal was received by an identical Ka-band antenna and filtered using the bandpass filter (BPF) (Marki, Morgan Hill, CA, USA), which has a center frequency of 27.38 GHz and a 3-dB passband of 8.3 GHz. After filtering, the signal at a central frequency of 28 GHz was amplified by the SAGE SBL low-noise amplifier (LNA) with a gain of 40 dB, allowing further processing in the mm-wave RAU receiver. The amplified signal was then sent to the envelope detector (Spacek Labs, Santa Barbara, CA, USA) with 13.5 GHz bandwidth, which performed frequency down-conversion of the 28 GHz intermediate frequency signal. The down-converted baseband signal was then sent to the digital storage oscilloscope (DSO) and the ESTT 7 Series [35] event timer via a custom-made low-pass filter (LPF) with a bandwidth of up to 1.8 GHz for analysis. This specific LPF [40] was purposefully utilized to broaden the received pulses for accurate detection with the ESTT, as the group delay of this filter remains nearly constant for frequencies up to 3 GHz, thus reducing pulse shape distortions. The magnitude response of the ARoF communication system, including the custom LPF, can be seen in Figure 6. Additionally, the Keysight DSOZ334A DSO, with a sample rate of 80 GSa/s and a bandwidth of 33 GHz, was initially used for signal visualization and optimization after wireless transmission and was later replaced with the ESTT for experimental measurements. The pulse waveforms for various pulse duration values  $\tau$ , captured by the DSO, for the back-to-back experimental setup and the setup involving 20 km SMF, can be seen in Figure 7 and Figure 8, respectively.

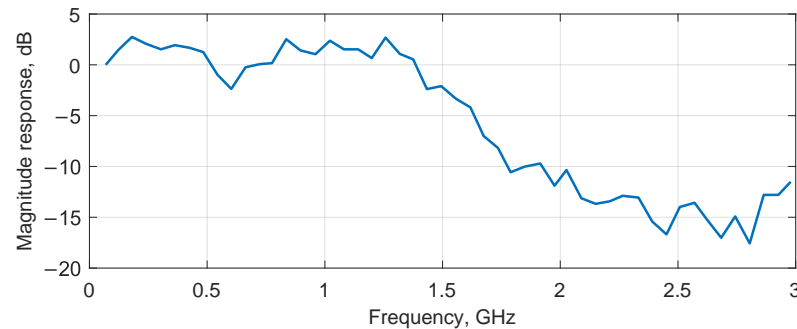


**Figure 6.** Magnitude response of the ARoF system.

As shown in Figures 7 and 8, the pulses after the LPF in the RAU receiver are broadened to approximately 500 ps, facilitating their detection by the ESTT. However, the expansion comes at the cost of the pulse waveform amplitude.

In the presented receiver RAU, ESTT is working as a TDC, triggering at the incoming pulses and converting the absolute times of the events into digital numerical values in ps, called “time tags”. ESTT uses a variable voltage threshold, which can be set by software in a range between  $-2$  V and 3 V with step 1.2 mV. In the case of PPM, where pulses are transmitted with high amplitude, this device successfully works as a TDC, as presented in Section 4 of this and our previous research [37].

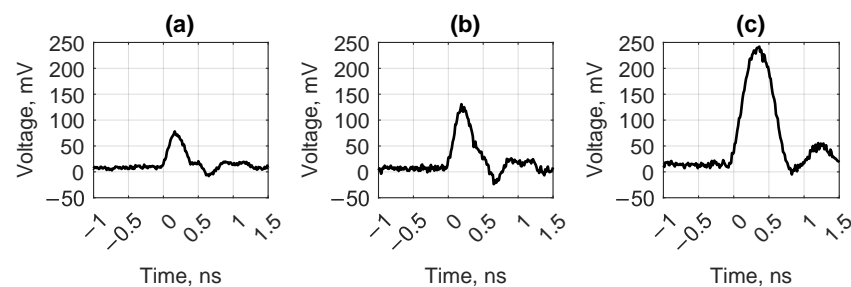


**Figure 7.** Pulse waveforms after the envelope detector for back-to-back experiment setup with (a)  $\tau = 100$  ps, (b)  $\tau = 200$  ps, (c)  $\tau = 500$  ps.

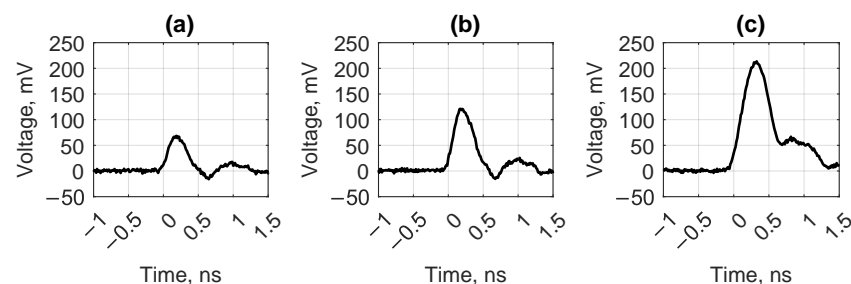


**Figure 8.** Pulse waveforms after the envelope detector for experiment setup with 20 km SMF with (a)  $\tau = 100$  ps, (b)  $\tau = 200$  ps, (c)  $\tau = 500$  ps.

ESTT is connected to the PC via a USB 3.0 interface, providing fast real-time transfer of time tags to PC. TR-PPM demodulation from time tags and forward error correction (FEC) is done in the receiver’s software part, written in C++20 and running on the PC.

### 3.4. Data Preparation

The transmitted data were generated as a  $1.224 \times 10^6$  bit long PRBS using the Mersenne Twister pseudo-random number generator with the order of 623, establishing a minimum detectable BER of  $8.17 \times 10^{-7}$  corresponding to a single error in the demodulated data. These data were saved for later comparison with the demodulated data. The TR-PPM

waveforms were generated offline in MATLAB 2024a with pulse durations varying from 500 ps to 100 ps and time bin durations ranging from 200 ps to 50 ps and then loaded into the AWG. The number of pulse positions was adjusted for each configuration to achieve optimal data rates for the given parameters [36]. Additionally, these waveforms were generated with and without ECC. Error correction was implemented using Gray code alone and Gray code with CCSDS “Blue book” 131.0-B-5 Section 4 standard-compliant RS ECC, which can correct up to 16 error bytes in the encoded data. In the case of RS encoding, the waveform was generated with the number of positions  $M = 256$ , so that one byte of data takes up an entire TR-PPM frame and is not split across multiple frames.

### 4. Experimental Results

Two sets of experiments were performed, with and without a 20 km SMF link and BER measurements were made with and without ECC. The results are presented in Figures 9 and 10 and summarized in Table 1. For error-free demodulation, the BER is reported as  $<8.17 \times 10^{-7}$ , as lower BER values cannot be measured with the given data set size.

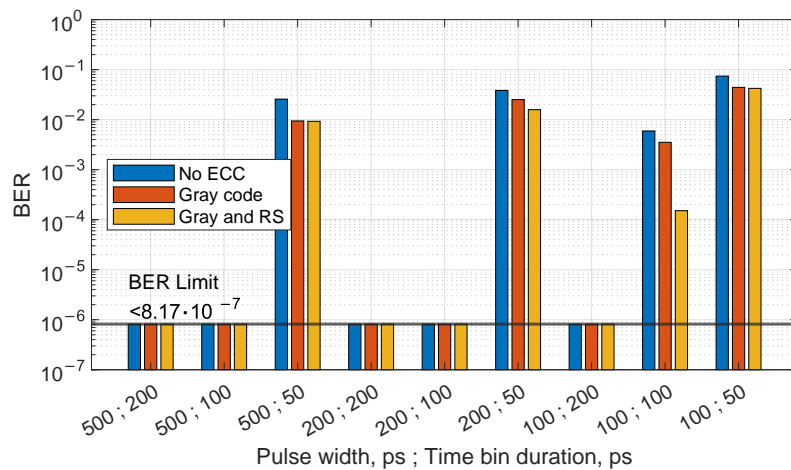


Figure 9. BER measurement results for TR-PPM transmission over ARoF experiments, using PRBS, for setup with 20 km SMF. Bars shown at BER limit  $8.17 \times 10^{-7}$  have 0 errors in the received data.

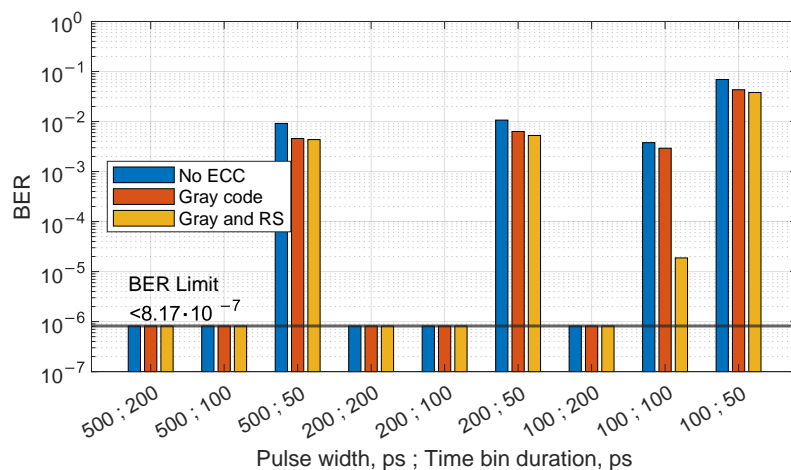


Figure 10. BER measurement results for TR-PPM transmission over ARoF experiments, using PRBS, for back-to-back setup. Bars shown at BER limit  $8.17 \times 10^{-7}$  have 0 errors in the received data.

All measurements with a time bin duration of 200 ps demonstrate error-free transmission. Error-free transmission was also achieved with both 500 ps and 200 ps pulse widths, using a time bin duration of 100 ps.

It can be seen that the employment of Gray code, which ensures that only one bit is flipped if the received pulse is located in the adjacent time bin, slightly decreases the BER, which is further reduced by the use of RS (255, 223) code. Employment of RS code significantly reduces the BER for measurements with the pulse width of 100 ps and time bin duration of 100 ps. For all measurements involving the time bin duration of 50 ps, the impact of RS code is negligible, which can be attributed to the high amount of flipped bits in the TR-PPM frames which carry the parity bytes. When considering time bin durations smaller than the pulse width, the effect of the additive noise is especially significant, as the detection threshold may be reached over a time span longer than the time bin duration in systems employing a timer-based TDC.

Comparing measurements with and without the 20 km SMF, the back-to-back measurements result in a lower overall BER than when the 20 km fiber is connected. BER degradation in the latter case can be attributed to dispersion in the fiber, which causes degradation of the pulse shape and a reduction in the steepness of the rising edge. This, in turn, increases sensitivity to additive noise, resulting in errors in pulse position measurements by the ESTT.

**Table 1.** Results of the TR-PPM transmission over ARoF experiments, using PRBS for back-to-back setup and setup with 20 km SMF.

ECC	Pulse Duration $\tau$ , ps	Time Bin Duration $\Delta$ , ps	Number of Positions $M$	20 km Fiber BER	Back-to-Back BER
No ECC	500	200	128	$<8.17 \times 10^{-7}$	$<8.17 \times 10^{-7}$
	500	100	256	$<8.17 \times 10^{-7}$	$<8.17 \times 10^{-7}$
	500	50	512	$2.578 \times 10^{-2}$	$9.169 \times 10^{-3}$
	200	200	128	$<8.17 \times 10^{-7}$	$<8.17 \times 10^{-7}$
	200	100	256	$<8.17 \times 10^{-7}$	$<8.17 \times 10^{-7}$
	200	50	512	$3.848 \times 10^{-2}$	$1.068 \times 10^{-2}$
	100	200	128	$<8.17 \times 10^{-7}$	$<8.17 \times 10^{-7}$
	100	100	256	$5.936 \times 10^{-3}$	$3.781 \times 10^{-3}$
	100	50	512	$7.436 \times 10^{-2}$	$6.931 \times 10^{-2}$
Gray code	500	200	128	$<8.17 \times 10^{-7}$	$<8.17 \times 10^{-7}$
	500	100	256	$<8.17 \times 10^{-7}$	$<8.17 \times 10^{-7}$
	500	50	512	$9.433 \times 10^{-3}$	$4.572 \times 10^{-3}$
	200	200	128	$<8.17 \times 10^{-7}$	$<8.17 \times 10^{-7}$
	200	100	256	$<8.17 \times 10^{-7}$	$<8.17 \times 10^{-7}$
	200	50	512	$2.518 \times 10^{-2}$	$6.317 \times 10^{-3}$
	100	200	128	$<8.17 \times 10^{-7}$	$<8.17 \times 10^{-7}$
	100	100	256	$3.524 \times 10^{-3}$	$2.924 \times 10^{-3}$
	100	50	512	$4.427 \times 10^{-2}$	$4.318 \times 10^{-2}$
Gray code and RS	500	200		$<8.17 \times 10^{-7}$	$<8.17 \times 10^{-7}$
	500	100		$<8.17 \times 10^{-7}$	$<8.17 \times 10^{-7}$
	500	50		$9.285 \times 10^{-3}$	$4.356 \times 10^{-3}$
	200	200		$<8.17 \times 10^{-7}$	$<8.17 \times 10^{-7}$
	200	100	256	$<8.17 \times 10^{-7}$	$<8.17 \times 10^{-7}$
	200	50		$1.584 \times 10^{-2}$	$5.267 \times 10^{-3}$
	100	200		$<8.17 \times 10^{-7}$	$<8.17 \times 10^{-7}$
	100	100		$1.514 \times 10^{-4}$	$1.875 \times 10^{-5}$
	100	50		$4.226 \times 10^{-2}$	$3.804 \times 10^{-2}$

The results strongly agree with previously published findings [40–42] in that in PPM data transmission, pulse shape plays a vital role in the overall system performance. The presented pulse waveforms after the RF transmission show distortions not dissimilar to

existing research on RoF systems, where waveforms were captured after the optical transmission network.

## 5. Conclusions

This research demonstrates the use of TR-PPM for data transmission in an ARoF system, with signal detection carried out by a commercial time tagger. The experimental results confirm the feasibility of this approach and highlight the potential of PPM over RoF for wireless communication applications, as well as the possibility of extending this concept to PPM-based ISAC implementations.

The primary factor influencing the performance of the ARoF TR-PPM communication system is the time bin duration, which directly determines the system's tolerance to jitter. The results validate the effectiveness of the implemented encoding algorithms, as enabling ECC reduces the BER in both the 20 km SMF and back-to-back setups. Tests with a 20 km SMF show only a slight BER increase over the back-to-back setup, which remains negligible for data transmission. In both configurations, multiple combinations of pulse widths and time bin durations resulted in a BER of  $<8.17 \times 10^{-7}$ , which is below the threshold corresponding to a single bit error after PPM signal demodulation. Within the context of this research, all BER values below this limit can be interpreted as error-free data transmission.

**Supplementary Materials:** The following supporting information can be downloaded at: <https://www.mdpi.com/article/10.3390/app15084222/s1>.

**Author Contributions:** Conceptualization, S.M., S.S. and T.S.; methodology, T.S. and O.O.; software, S.M. and N.T.; validation, S.M., N.T., S.S. and K.R.; formal analysis, S.M. and K.R.; investigation, K.R., S.M. and N.T.; resources, A.A., S.S., V.B. and O.O.; data curation, S.M., N.T. and K.R.; writing—original draft preparation, S.M., K.R. and N.T.; writing—review and editing, A.A., S.M., N.T. and S.S.; visualization, N.T. and S.M.; supervision, A.A. and V.B.; project administration, A.A.; funding acquisition, A.A. All authors have read and agreed to the published version of the manuscript.

**Funding:** This research was funded by the Latvian Council of Science grant No. lzp-2021/1-0475, "Picosecond-resolution pulse position modulation for beyond-the-limits energy efficiency of communications".

**Institutional Review Board Statement:** Not applicable.

**Informed Consent Statement:** Not applicable.

**Data Availability Statement:** The original contributions presented in this study are included in the article and Supplementary Materials. Further inquiries can be directed to the corresponding author.

**Conflicts of Interest:** The authors declare no conflict of interest.

## Abbreviations

The following abbreviations are used in this manuscript:

ADC	analog-to-digital converter
ARoF	analog radio-over-fiber
AU	antenna unit
AWG	arbitrary waveform generator
BER	bit error ratio
BPF	bandpass filter
CCSDS	Consultative Committee for Space Data Systems
CW	continuous wave
DAC	digital-to-analog converter
D-MIMO	distributed multiple-input multiple-output

DSO	digital storage oscilloscope
ECC	error correcting code
EDFA	erbium-doped fiber amplifier
ESRTM	Eventech Space Ready Timing Module
ESTT	Eventech Stream Time Tagger
FEC	forward error correction
FSO	free-space optical communication
FWM	four-wave mixing
IR-UWB	impulse radio ultra-wideband
ISAC	integrated sensing and communications
LNA	low-noise amplifier
LPF	low-pass filter
MZM	Mach-Zehnder modulator
NOE	nonlinear optical effects
OOK	on-off keying
PIN	p-i-n photodiode
PPM	pulse position modulation
PRBS	pseudorandom binary sequence
QAM	quadrature amplitude modulation
QSSB-UWB	quasi single-sideband UWB
RAU	remote antenna unit
RF	radio frequency
RMS	root mean square
RoF	radio-over-fiber
RS	Reed-Solomon
SMF	single-mode optical fiber
TDC	time-to-digital converter
TR-PPM	transmitted reference PPM
UWB	ultra-wideband

## References

1. ITU-R. *Report ITU-R M.2516-0: Future Technology Trends of Terrestrial International Mobile Telecommunications Systems Towards 2030 and Beyond*; ITU-R: Geneva, Switzerland, 2022.
2. Wikström, G.; Peisa, J.; Rugeland, P.; Johansson, N.; Parkvall, S.; Girnyk, M.; Mildh, G.; Da Silva, I.L. Challenges and Technologies for 6G. In Proceedings of the 2020 2nd 6G Wireless Summit (6G SUMMIT), Levi, Finland, 17–20 March 2020; pp. 1–5. [\[CrossRef\]](#)
3. Lim, C.; Tian, Y.; Ranaweera, C.; Nirmalathas, T.A.; Wong, E.; Lee, K.L. Evolution of Radio-Over-Fiber Technology. *J. Light. Technol.* **2019**, *37*, 1647–1656. [\[CrossRef\]](#)
4. Puerta, R.; Jiang, T.; Joharifar, M.; Ostrovskis, A.; Salgals, T.; Rubuls, K.; Schatz, R.; Djupsjöbacka, A.; Pittalà, F.; Gruen, M.; et al. Analog Mobile Fronthaul for 6G and Beyond. *J. Light. Technol.* **2024**, *42*, 7458–7467. [\[CrossRef\]](#)
5. Ostrovskis, A.; Salgals, T.; Rubuls, K.; Skladova, L.; Bobrovs, V.; Spolitis, S. Experimental Demonstration of Hybrid Photonics-Based ARoF System for 5G and B5G Networks. In Proceedings of the 2022 International Conference on Software, Telecommunications and Computer Networks (SoftCOM), Split, Croatia, 22–24 September 2022; pp. 1–5. [\[CrossRef\]](#)
6. Jiang, W.; Schotten, H.D. Full-Spectrum Wireless Communications for 6G and Beyond: From Microwave, Millimeter-Wave, Terahertz to Lightwave. In Proceedings of the 2023 IEEE 3rd International Conference on Computer Communication and Artificial Intelligence (CCAI), Taiyuan, China, 26–28 May 2023; pp. 353–357. [\[CrossRef\]](#)
7. Li, W.; Yu, J.; Ji, X.; Liu, J.; Wang, F.; Zhu, B.; Zhou, W.; Zhao, F.; Yu, J. Over 100 Gb/s mm-wave delivery with 4600 m wireless distance based on dual polarization multiplexing. *Sci. China Inf. Sci.* **2023**, *66*, 1869–1919. [\[CrossRef\]](#)
8. Jia, S.; Lo, M.C.; Zhang, L.; Ozolins, O.; Udalcovs, A.; Kong, D.; Pang, X.; Guzman, R.; Yu, X.; Xiao, S.; et al. Integrated Dual-Laser Photonic Chip for High-Purity Carrier Generation Enabling Ultrafast Terahertz Wireless Communications. *Nat. Commun.* **2022**, *13*, 1388. [\[CrossRef\]](#) [\[PubMed\]](#)
9. Jiang, T.; Rubuls, K.; Joharifar, M.; Ostrovskis, A.; Djupsjöbacka, A.; Salgals, T.; Zvěřina, J.; Halmo, L.; Spolitis, S.; Bobrovs, V.; et al. Photonics-Enabled 6G Distributed MIMO: Experimental Study in an Indoor Environment. In Proceedings of the 2024 International Topical Meeting on Microwave Photonics (MWP), Pisa, Italy, 17–20 September 2024; pp. 1–5. [\[CrossRef\]](#)
10. Yao, J. Microwave Photonics. *J. Light. Technol.* **2009**, *27*, 314–335. [\[CrossRef\]](#)

11. Anes, B.; Riad, B.A. A new bidirectional analog radio over fiber transmission for 5G millimeter wave communication systems. In Proceedings of the 2022 International Conference of Advanced Technology in Electronic and Electrical Engineering (ICATEEE), M'sila, Algeria, 26–27 November 2022; pp. 1–6. [[CrossRef](#)]
12. Perez-Galacho, D.; Sartiano, D.; Sales, S. Analog Radio over Fiber Links for Future 5G Radio Access Networks. In Proceedings of the 2019 21st International Conference on Transparent Optical Networks (ICTON), Angers, France, 9–13 July 2019; pp. 1–4. [[CrossRef](#)]
13. Delmade, A.; Vargas, C.; Kearney, A.; Nellen, S.; Kohlhaas, R.B.; Schell, M.; Coffey, D.; Smyth, F.; Barry, L.P. Expanded Gain-Switched Comb Source for 180–260 GHz Sub-THz Analog Radio-over-Fiber 6G Wireless System. In Proceedings of the 2024 Optical Fiber Communications Conference and Exhibition (OFC), San Diego, CA, USA, 24–28 March 2024; pp. 1–3.
14. de Souza Lopes, C.H.; Saia Lima, E.; Sodr e Junior, A.C. RoF/FSO-based Fronthaul for 5G Systems and Beyond. In Proceedings of the 2021 SBMO/IEEE MTT-S International Microwave and Optoelectronics Conference (IMOC), Fortaleza, Brazil, 24–27 October 2021; pp. 1–3. [[CrossRef](#)]
15. Nguyen, D.N.; Bohata, J.; Komanec, M.; Zvanovec, S.; Ortega, B.; Ghassemlooy, Z. Optical Hybrid Fiber/Free-Space and 25 GHz Wireless Transmission Using LTE M-QAM Signals. In Proceedings of the 2019 22nd International Symposium on Wireless Personal Multimedia Communications (WPMC), Lisbon, Portugal, 24–27 November 2019; pp. 1–6. [[CrossRef](#)]
16. Azizpour, R.; Zakeri, H.; Moradi, G.; Alibakhshikenari, M.; Falcone, F.; Liu, B.; Dendini, T.A.; Park, I.; Koziel, S.; Limiti, E. Multi-Channel Radio-Over-Fiber Communication Systems Through Modulation Instability Phenomenon. *IEEE Photonics J.* **2024**, *16*, 7201813. [[CrossRef](#)]
17. Jia, Z.; Yu, J.; Chang, G.K. A Full-Duplex Radio-over-Fiber System Based on Optical Carrier Suppression and Reuse. *IEEE Photonics Technol. Lett.* **2006**, *18*, 1726–1728. [[CrossRef](#)]
18. Yang, L.; Giannakis, G. Ultra-wideband communications: An idea whose time has come. *IEEE Signal Process. Mag.* **2004**, *21*, 26–54. [[CrossRef](#)]
19. Al Zaman, A.; Islam, N. Modulation Schemes and Pulse Shaping in Ultra-Wideband. In Proceedings of the IEEE SoutheastCon 2008, Huntsville, AL, USA, 3–6 April 2008; pp. 142–146. [[CrossRef](#)]
20. Huo, X.; Xiang, M.; Zhou, G.; Li, J.; Li, J.; Qin, Y.; Fu, S. C-Band 200 Gbit/s/ $\lambda$  PS-PAM-8 Transmission Over 2-km SSMF for Optical Interconnections. *IEEE Photonics J.* **2024**, *16*, 7200807. [[CrossRef](#)]
21. Pan, S.; Yao, J. UWB-Over-Fiber Communications: Modulation and Transmission. *J. Light. Technol.* **2010**, *28*, 2445–2455. [[CrossRef](#)]
22. Pan, S.; Yao, J. Performance evaluation of UWB signal transmission over optical fiber. *IEEE J. Sel. Areas Commun.* **2010**, *28*, 889–900. [[CrossRef](#)]
23. Abraha, S.T.; Okonkwo, C.; Yang, H.; Visani, D.; Shi, Y.; Jung, H.D.; Tangdionga, E.; Koonen, T. Performance Evaluation of IR-UWB in Short-Range Fiber Communication Using Linear Combination of Monocycles. *J. Light. Technol.* **2011**, *29*, 1143–1151. [[CrossRef](#)]
24. Kaszubowska-Anandarajah, A.; Perry, P.; Barry, L.P.; Shams, H. An IR-UWB Photonic Distribution System. *IEEE Photonics Technol. Lett.* **2008**, *20*, 1884–1886. [[CrossRef](#)]
25. Fujiwara, Y. Self-Synchronizing Pulse Position Modulation With Error Tolerance. *IEEE Trans. Inf. Theory* **2013**, *59*, 5352–5362. [[CrossRef](#)]
26. Mahdiraji, G.A.; Zahedi, E. Comparison of Selected Digital Modulation Schemes (OOK, PPM and DPIM) for Wireless Optical Communications. In Proceedings of the 2006 4th Student Conference on Research and Development, Shah Alam, Malaysia, 27–28 June 2006; pp. 5–10. [[CrossRef](#)]
27. Li, L.; Townsend, J.K. M-Ary PPM for Transmitted Reference Ultra-Wideband Communications. *IEEE Trans. Commun.* **2010**, *58*, 1912–1917. [[CrossRef](#)]
28. Luo, X.; Giannakis, G. Achievable Rates of Transmitted-Reference Ultra-Wideband Radio with PPM. *IEEE Trans. Commun.* **2006**, *54*, 1536–1541. [[CrossRef](#)]
29. Aliaberi, A.; Sofotasios, P.C.; Muhaidat, S. Modulation Schemes for Visible Light Communications. In Proceedings of the 2019 International Conference on Advanced Communication Technologies and Networking (CommNet), Rabat, Morocco, 12–14 April 2019; pp. 1–10. [[CrossRef](#)]
30. Dahri, F.A.; Ali, S.; Jawaid, M.M. A Review of Modulation Schemes for Visible Light Communication. *IJCSNS Int. J. Comput. Sci. Netw. Secur.* **2018**, *18*, 117–125.
31. Mietzner, J.; Lampe, L. Nested PPM for Visible Light Communication with Heterogeneous Optical Receivers. *IEEE Photonics J.* **2024**, *16*, 7302112. [[CrossRef](#)]
32. Alabd, M.B.; Nuss, B.; de Oliveira, L.G.; Diewald, A.; Li, Y.; Zwick, T. Modified Pulse Position Modulation for Joint Radar Communication Based on Chirp Sequence. *IEEE Microw. Wirel. Compon. Lett.* **2022**, *32*, 1247–1250. [[CrossRef](#)]
33. Guelman, M.; Kogan, A.; Kazarian, A.; Livne, A.; Orenstein, M.; Michalik, H. Acquisition and Pointing Control for Inter-Satellite Laser Communications. *IEEE Trans. Aerosp. Electron. Syst.* **2004**, *40*, 1239–1248. [[CrossRef](#)]

34. Colson, S.; Hoff, H. Ultra-Wideband Technology for Defence Applications. In Proceedings of the 2005 IEEE International Conference on Ultra-Wideband, Zurich, Switzerland, 5–8 September 2005; pp. 615–620. [CrossRef]
35. Eventech. Key Products. Available online: <https://eventechsite.com/products/> (accessed on 27 March 2025).
36. Selis, O.; Migla, S.; Sics, P.E.; Zeltins, M.; Spolitis, S.; Aboltins, A. Demonstration of 50 ps Per-Position Differential Pulse Position Modulation Data Transmission. In Proceedings of the 2023 IEEE 10th Jubilee Workshop on Advances in Information, Electronic and Electrical Engineering (AIEEE), Vilnius, Lithuania, 27–29 April 2023; pp. 1–4. [CrossRef]
37. Sics, P.E.; Tihomorskis, N.; Migla, S.; Ratners, J.; Kurtenoks, V.; Aboltins, A. Implementation of Reconfigurable 149 Mbps TDC-Based PPM Transceiver. In Proceedings of the 2024 Joint European Conference on Networks and Communications & 6G Summit (EuCNC/6G Summit), Antwerp, Belgium, 3–6 June 2024; pp. 706–710. [CrossRef]
38. Eventech. Eventech Space Ready Timing Module. Available online: <https://eventechsite.com/wp-content/uploads/2024/08/Eventech-Space-Ready-Timing-Module-2024.pdf> (accessed on 27 March 2025).
39. European Space Agency. Hera’s Asteroid Deck and instruments. Available online: [https://www.esa.int/Space\\_Safety/Hera/Hera\\_s\\_Asteroid\\_Deck\\_and\\_instruments](https://www.esa.int/Space_Safety/Hera/Hera_s_Asteroid_Deck_and_instruments) (accessed on 27 March 2025).
40. Aboltins, A.; Solovjova, T.; Semenako, J.; Kusnins, R.; Migla, S.; Sics, P.E.; Selis, O.; Tihomorskis, N.; Prigunovs, D.; Ostrovskis, A.; et al. Passive Electrical and Optical Methods of Ultra-Short Pulse Expansion for Event Timer-Based TDC in PPM Receiver. *Electronics* **2023**, *12*, 4634. [CrossRef]
41. Liu, Y.; Wang, C. The Research on Transmission Effect of Different Pulse Shapes in MPPM. In Proceedings of the 2022 14th International Conference on Computer Research and Development (ICCRD), Shenzhen, China, 7–9 January 2022; pp. 373–377. [CrossRef]
42. Cho, S.; Kwak, J. Performance Comparison of M-Ary PPM Ultra-Wideband Multiple Access System Using an Intelligent Pulse Shaping Techniques. In *International Conference on Knowledge-Based and Intelligent Information and Engineering Systems*; Springer: Berlin/Heidelberg, Germany, 2005; pp. 1094–1103.

**Disclaimer/Publisher’s Note:** The statements, opinions and data contained in all publications are solely those of the individual author(s) and contributor(s) and not of MDPI and/or the editor(s). MDPI and/or the editor(s) disclaim responsibility for any injury to people or property resulting from any ideas, methods, instructions or products referred to in the content.